1

OBSERVATIONS IN THE SHADOW OF MARS BY THE NEUTRAL PARTICLE IMAGER

M. Holmström^{1,2}, K. Brinkfeldt¹, S. Barabash¹, and R. Lundin¹

Swedish Institute of Space Physics

P.O. Box 812, SE-98128 Kiruna, Sweden

Currently at NASA Goddard Space Flight Center

Code 612.2, Greenbelt, MD 20771, USA

E-mail: matsh@irf.se

We present observations of energetic neutral atoms (ENAs) in the shadow of Mars by the neutral particle imager (NPI), part of the ASPERA-3 experiment on-board Mars Express. The observations are well into the umbra, where the count rates are low, and contamination by UV light minimal. We present statistics over all available observations, from the 2004 and the early 2005 eclipse seasons. We investigate skymaps of the observations, and their time dependence, and try infer the different origins of the observed fluxes: instrumental effects, ENAs from Mars and its interaction with the solar wind, and ENAs of possibly heliospheric origin. We also study the time evolution of the observed signals. It is found that most of the observed emissions are consistent with UV, but some are not, suggesting ENA fluxes — Mars related and non-Mars related.

The NPI measure the integral ENA flux (0.1–60 keV) with no mass or energy resolution, but with high angular resolution (5 \times 11 degrees). The sensor is also sensitive to UV light.

1. Introduction

The Neutral Particle Imager (NPI) is part of the ASPERA-3 experiment¹ on-board the European Space Agency's Mars Express mission (MEX) that was launched on June 2, 2003, and entered orbit around the planet early on Christmas morning 2003.

The ASPERA-3 instrument is comprised of four sensors; two ENA sensors, an electron spectrometer and an ion mass spectrometer.

The NPI provides measurements of the integral energetic neutral atom (ENA) flux with no mass or energy resolution but high angular resolution. The sensor utilizes reflection and ion sputtering from a graphite surface to detect ENAs and suppress the UV background. NPI is a replica of the ENA sensor used in the ASPERA-C experiment on the Mars-96 mission² and was successfully flown on the Swedish microsatellite Astrid³, launched

in 1995. The UV suppression is not perfect, and we will later discuss how to separate ENAs from UV in the data.

The second ENA sensor, the neutral particle detector (NPD), provides measurements of the ENA flux, resolving velocity and mass (H and O) with a coarser angular resolution. ENAs incident on a surface at a grazing angle of 15° are reflected and cause secondary electrons used for a start signal. The reflected ENAs hit a second surface and again produce secondary electrons utilized for a stop signal. Time-of-flight electronics give the ENA velocity. The pulse-height distribution of the stop signals roughly determine the ENA mass. The NPD sensor is a new development.

ASPERA-3 provides the first ever ENA measurements in the solar wind energy range at another planet. In this work we describe, and discuss, NPI measurements in the shadow of Mars during the 2004 and early 2005 eclipse seasons.

2. Background

The NPI measure the integral ENA flux (in the energy range 0.1-60 keV) with no mass or energy resolution, but with good angular resolution. The incoming ENAs are detected by 32 sectors in a plane for a 360 degree field of view (FOV), with a 5 degree FOV perpendicular to the plane. Here we number the sectors from 0 to 31. The direction between sector 0 and 31 is NPI's x-axis, along the Mars Express z-axis that points toward the center of the planet during nadir observations. Sectors 15 and 16 are physically blocked and the count rates should be on the noise level, but we see higher count rates in the data from these sectors. This is an instrumental effect that is not yet understood, and these sectors should be disregarded if they appear in any plot (they are not used in any of the analysis of this paper).

The time resolution is one second, so the raw data is 30 integer counts every second. ASPERA-3's main unit is mounted on a scanning platform which means that the NPI can rotate around its x-axis when the scanner is operated. Here we will only discuss observations when the scanner was not operated. Then NPI is fix relative the spacecraft with its FOV plane perpendicular to MEX's y-axis (and the axis of the solar panels). Sector 8 is looking in the general direction of MEX x-axis (and the high-gain antenna). An illustration of the NPI geometry is shown in Fig. 1.

During different parts of Mars Express polar orbit, and during different Martian seasons, the NPI samples different ENA populations. NPI dayside observations have been reported by Gunell⁴, and Brinkfeldt⁵ and Kallio⁶

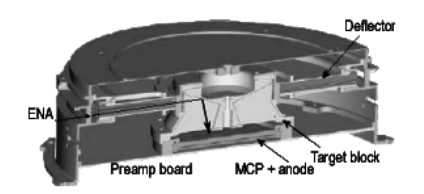


Fig. 1. Illustration of the NPI geometry.

have investigated the decrease and increase in ENA flux at entry and exit of the Martian shadow. Predictions by computer simulations of the ENA generation from solar wind protons⁷ and photoionized planetary oxygen⁸ has previously been done. Here we investigate the ENA fluxes in Mars' umbra. One motivation is to search for interplanetary ENA populations. The interstellar neutral stream of helium, as detected by the ULYSSES/GAS-instrument⁹, is of too low energy (13 eV) to be detected by the NPI, since the NPI only is sensitive to neutrals with an energy of at least 200 eV (see Fig. 11) and the energy of the interstellar neutral helium will be below this energy even if we account for Mars' orbital velocity, and the gravitational acceleration of Mars and the Sun.

However, many different observations hint at the existence of other interplanetary fluxes of neutral atoms (no direct observations have been made), as described by Collier et al¹⁰. Such streams might have energies in the keV range, detectable by the NPI. The most promising part of Mars Express' orbit to search for such streams is in the shadow of the planet since we then do not have any direct solar UV light contamination, and the flux of ENAs from the Mars-solar wind interaction should be low.

In Fig. 2 we see an example of the raw data from an eclipse observation.

Mars Express' orbit goes into the shadow at different time periods (eclipse seasons). The data analyzed here is from two different eclipse seasons, one in 2004 and one in early 2005. This is summarized in Table 1. Fig. 3 shows the eclipse part of the orbit, and how it evolves during these two eclipse seasons.

To avoid the ENA fluxes at entry and exit of eclipses (probably ENAs produced by solar wind-exosphere charge exchange that then are scattered by elastic collisions in the exosphere) we restrict the examined data to observations when the spacecraft is at least 0.15 Martian radii inside the

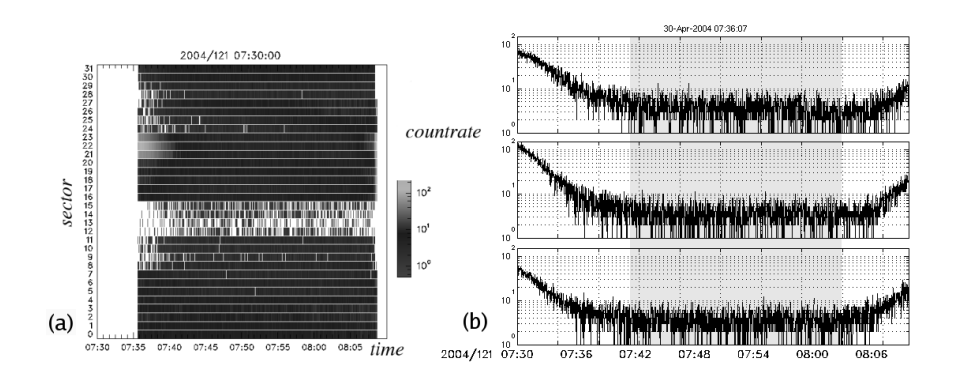


Fig. 2. Typical NPI eclipse observation on April 30, 2004, 07:36 to 08:08. (a) Countrates for all 32 sectors as a function of time. Sector 31 is the top row and sector 0 at the bottom. We see the sun set in sector 12 early in the observation, and rise again at the end of the observation. (b) Countrates for three of the sectors with the deep eclipse region shaded. The sectors are 21, 22 and 23 from top to bottom. The y-axis scale goes up to 100 counts per second.

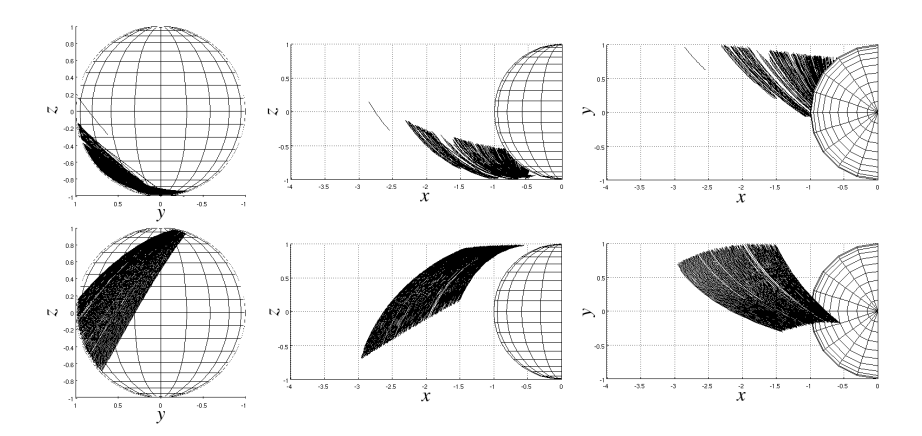


Fig. 3. Eclipse orbit geometry for the NPI observations during 2004 (top) and early 2005 (bottom). The time periods correspond to the dates given in Table 1. From left to right the yz-, xz-, and xy-planes in the Mars Solar Orbital (MSO) coordinate system, where the x-axis is toward the Sun, the z-axis is perpendicular to the planet's velocity, in the northern ecliptic hemisphere, and the y-axis completes the right handed system (and is approximately opposite to Mars' velocity vector).

umbra (if not otherwise noted). We call these observations deep umbra observations. The value of 0.15 was chosen after examining how the count rates depend on distance inside the umbra for all the observations. It was

Table 1. Summary of eclipse observations presented in this work.

Dates	Number of observations	Duration of eclipses	Mars' ecliptic longitude [deg]
2004-04-09 to 2004-08-21	259	10-20 min	102-162
2005-02-14 to 2005-03-31	163	30-60 min	245-270

found that the countrates level off inside this region, as illustrated in Fig. 2b. Examples of NPI's FOV in ecliptic coordinates are shown in Fig. 4 with Mars' limb and center also indicated. During Earth communication the NPI FOV plane is in the ecliptic plane. During nadir observations, inertial observations, and slews, the NPI observes other directions.

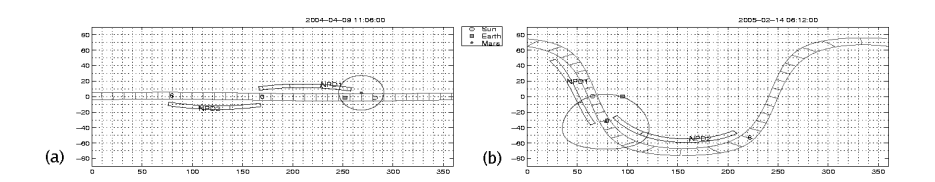


Fig. 4. Examples of NPI FOVs for eclipse observations in (a) 2004 and (b) 2005. The coordinate system is ecliptic with longitudes on x-axes, and latitudes on y-axes. The 32 NPI sectors' FOVs (look directions) is the continuous band with sector 0 and 8 indicated. For comparison, the FOVs of the six NPD sectors are also shown. Mars limb is the closed line with the planet center indicated. The sun direction is shown by a small disc, and Earth by a square. We can note that MEX is in Earth communication pointing in (a) and nadir pointing in (b).

To examine the NPI observations in ecliptic coordinates we would like to make sky maps where all the sectors contribute. A complication is that different sectors have different responses to ENAs. Their sensitivity and background noise levels are different. We can use ground calibration values to solve this inter-sector normalization problem, but we think that the inflight values are slightly different, and that they have changed between 2004 and 2005. Here we use ground calibration values for the sectors' relative sensitivities, and we compute the noise level (dark currents) for each sector from observations, as shown and explained in Table 2. The noise level was estimated by binning the eclipse observations in 60 second bins, and the smallest average count rate was chosen as a noise level estimate for each season. It would have been preferable to also do an in-flight estimate of the the sectors' relative sensitivities, and attempts has been made, e.g., to

identify times when different sectors look in the same direction close in time, but no good estimates were achieved. There is also priority effect due to

Table 2. Inter-sector normalizations. The normalized counts for sector i, v_i , is computed from the raw counts, u_i , as $v_i = (u_i - \alpha_i)/\beta_i$. The relative sensitivities, β_i , are from ground calibrations, and the off-sets (dark currents), α_i , are estimated from minimum deep umbra count rates averaged in 60 second bins, for respective year.

Sector i	0	1	2	3	4	5	6	7	8	9	10	11	12	13	14
β_i	1.11	1.07	1.08	1.07	1.00	0.99	1.10	1.04	1.00	1.31	1.30	1.16	1.05	0.85	0.88
α_i 2004	5.8	5.6	7.2	7.2	4.2	2.1	2.6	2.1	2.2	1.2	1.4	1.4	0.43	0.28	0.33
α_i 2005	10.3	9.2	11.5	12.6	5.9	3.4	3.9	3.9	3.1	1.4	1.5	1.4	0.20	0.17	0.15
Sector i	17	18	19	20	21	22	23	24	25	26	27	28	29	30	31
β_i	0.65	0.69	0.58	0.64	0.64	0.84	0.97	0.99	0.98	1.15	1.28	1.30	1.44	1.09	0.86
α_i 2004	1.9	2.3	3.4	2.1	1.3	1.6	1.8	1.3	1.2	1.4	1.7	0.62	1.2	1.2	1.8
α_i 2005	1.5	1.3	1.8	0.68	0.45	0.52	0.85	1.2	1.3	1.3	1.6	0.3	0.18	0.23	0.70

the electronics, where some counts are shifted to higher numbered sectors that we have not attempted to compensate for in the present analysis. This effect can be viewed as a reduction of the in-plane angular resolution of the sensor, since we get a smoothing between adjacent sectors. During calibrations, the effect was responsible for moving approximately 40% of the counts in sector n to sector n+1.

The position of the spacecraft and the look directions of the NPI sectors as a function of time were computed using the CSPICE¹¹ subroutine package. The raw data was processed using pkttool-1.103. The data and geometry information was merged into a text file that subsequently was read into Matlab for further processing and display. The software is available from the authors upon request.

3. Observations

Using the inter-sector normalization described in the previous section, we can compute skymaps for the NPI deep eclipse data that show the average count rate as a function of look direction ecliptic longitude and latitude. For each one-second observation, we first do an inter-sector normalization, according to Table 2, of the counts from each sector, then deposit the count in the cell that corresponds to the sector's boresight direction, and also accumulate the observation time on the grid. This is done for all the data to be included. In Fig. 5 we show the logarithm of the total time and

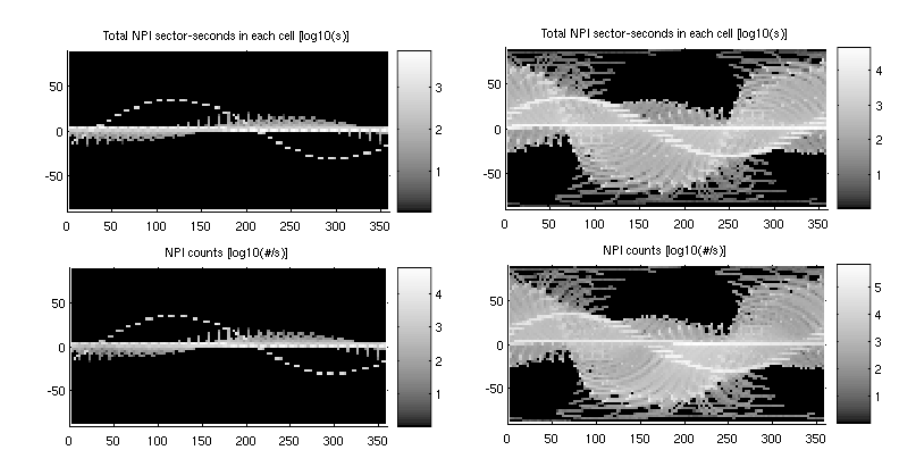
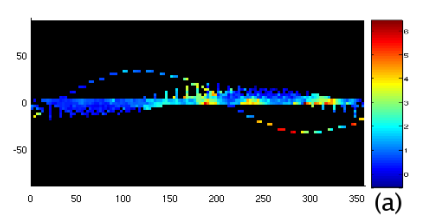


Fig. 5. Logarithmic sky maps of total sector time for each cell (top) and total number of counts (bottom) for NPI eclipse observations in 2004 (left) and 2005 (right). The coordinate system is ecliptic with longitudes on x-axes, and latitudes on y-axes, and the grid is 128×64 cells. Note the different color scales. Black denotes no coverage.

counts accumulated for each cell on the longitude–latitude grid. Finally, by dividing the accumulated counts in each cell by the total observation time we get an average count rate.

Such sky maps for 2004 and 2005 are shown in Fig. 6. In 2004 we note signals from the general Mars direction (see Fig. 4 for Mars' approximate location). These are probably charge exchange ENAs from the Mars-solar wind interaction and UV scattered and refracted in Mars' atmosphere. In this coordinate system, Mars will not have constant size and position during an orbit and from orbit to orbit, but for the deep umbra data the change is small (Mars can increase in apparent size by 50 degrees) and does not affect the different signals discussed later on. Another signal is seen coming from Mars' ram direction (the direction of the planets velocity vector) around 200° longitude. We will get back to this signal in the 2005 data. Note that there is also a signal from below the ecliptic near 0 longitude. We also see that the coverage out of the ecliptic is sparse during 2004. The cell size of the longitude-latitude grid was chosen smaller than the sector FOV (128×64 cells). Since we have many observations, we can achieve this superresolution. In 2005 we have more observations away from the ecliptic plane and we directly see the very strong emissions from below the ecliptic plane. These correspond well with the galactic plane.

The different characteristics of the individual sectors (sensitivity and



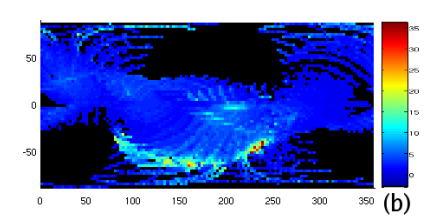


Fig. 6. Sky maps of average count rates [1/s] for NPI eclipse observations in 2004 (left) and 2005 (right), i.e. we see the average count rate that the NPI sectors have registered when pointing in that direction. The coordinate system is ecliptic with longitudes on x-axes, and latitudes on y-axes, and the grid is 128×64 cells. Note the different color scales. The maximum value on the colorbar is 6 in 2004, and 35 in 2005. Black denotes no coverage.

noise level as discussed in the previous section) in a way make the NPI composed of 30 different sensors. Therefore, one has to be careful when comparing observations from different sectors. That the strong signals seen in the sky maps are not artifacts of the normalization and averaging of different sectors has been checked by identifying the signals in the time serie of individual sectors, and it is also possible to see the features discussed if one looks at sky maps for individual sectors.

4. Analysis

The big question to try and answer is what signals are from ENAs and what are from UV? What is neutrals and what is photons? Some approaches to separate UV and ENA signals are

- Compare the observed sky maps with UV sky maps.
- Examine the time evolution of the signals. Stellar UV sources should be stable in position and intensity over time.
- Examine data from other ENA detectors to identify similar signals.
 Assuming an hydrogen ENA signal in the 1 keV range, the current possibilities are the NPD on MEX and LENA¹² on IMAGE. This is a topic for future studies.

Below we will address the first two items, but first of all: Could we be seeing something else than ENAs or UV, e.g., X-rays? Probably not, comparison with published sky maps in other wavelengths show no similarities to the features in Fig. 6.

Let us now compare the NPI skymaps in Fig. 6 with a UV skymap. In Fig. 7 we show SOHO/SWAN UV sky maps¹³. To the left in ecliptic and to the right in galactic coordinates. At the top is the original data, and at the bottom the same data smoothed by an NPI sector angular response function Appendix A. The Milky Way is clearly visible both in the

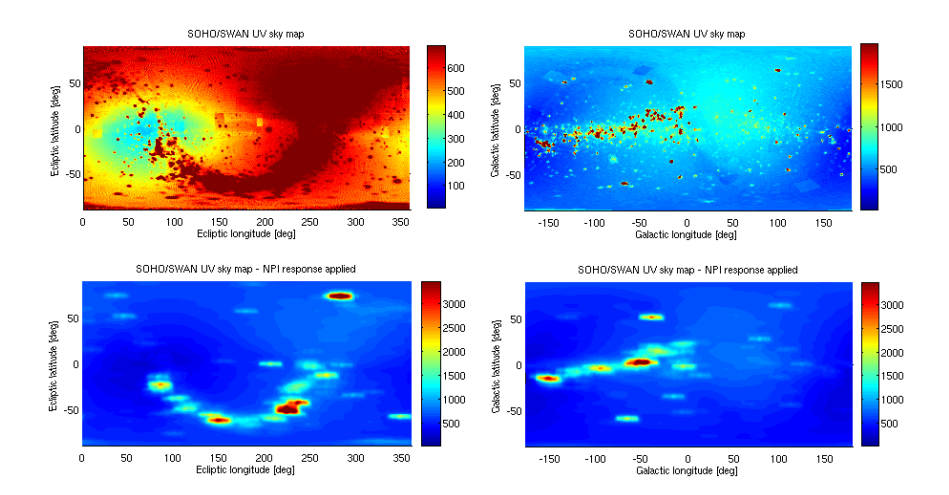


Fig. 7. SOHO/SWAN all-sky UV Maps on one degree resolution longitude-latitude grids in the unit of Rayleighs. The instrument is sensitive to the wavelengths 117-180 nm. The top row shows the raw images and in the bottom row we have convolved the images with the response function of one NPI sector (from calibrations). The left column is in ecliptic coordinates, and the right is in galactic coordinates. Note that the intensity ranges in the plots were chosen to enhance the features. The maximum in the raw images is $65~\mathrm{kR}$ and $5~\mathrm{kR}$ in the smoothed images. Data provided by Teemu Mäkinen on behalf of the SWAN team.

UV and NPI skymaps. In ecliptic coordinates it is the U-shaped structure. We can note that by comparing countrates in Fig. 6 and intensity in In Fig. 7 we can estimate the UV response of the NPI: 1 kR (uniformly over a sector) corresponds approximately to 10 counts per second, assuming that the galactic emissions are only UV. We can also compare the lower right plate in Fig. 6 with the NPI sky-map in galactic coordinates shown in Fig. 8. Most of the strong UV signals in the galactic plane correspond well to the NPI measurements. The UV source at longitude -150 is however an exception.

Turning now to the time evolution of the observed signals. We see in Fig. 6 that there is a source in the ecliptic around longitude 200 degrees

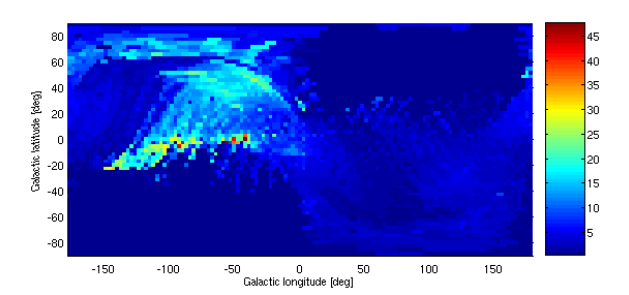


Fig. 8. The NPI skymap for 2005 in galactic coordinates (longitude-latitude). Otherwise the same as Fig. 6 (b).

in 2004 and 2005. However, it has moved to a higher longitude by approximately 25 degrees from 2004 to 2005, if it is the same signal. However, this shift is inconsistent with a UV source.

We further investigate the time evolution by examining how the ecliptic plane signals evolve over time in Fig. 9. Both years seem to include signals that are constant in longitude (suggesting UV) and change longitude at the same rate as the Sun (maybe Mars related), but also other changes are visible (possible ENAs), e.g., the emissions around longitude 200 look different in 2004 and 2005, and do also vary over time. In Fig. 10 we show

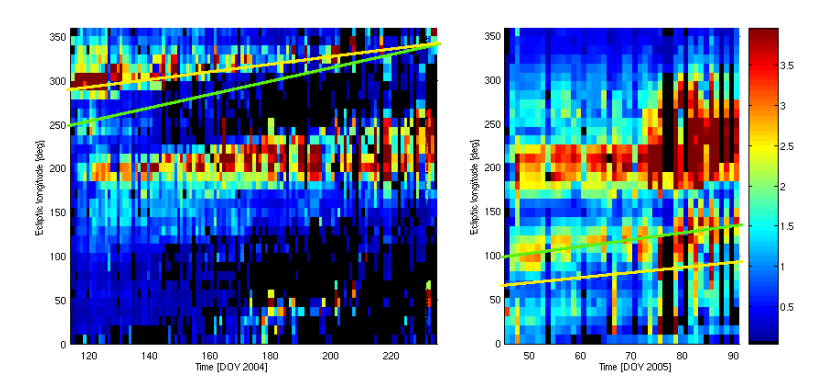


Fig. 9. Time evolution of the signal in the Ecliptic plane during 2004 (left) and 2005 (right). Each column represent average count rates [1/s] during one day. The x-axes are day of year, and the y-axes are ecliptic longitudes. Only observations by sectors looking at most 6 degrees off the ecliptic plane were included. For 2004 we included all umbra observations. The dark lines represent Earth's longitude, and the light lines the Sun's longitude.

how the galactic plane signals evolve over time. We see a clear change of the signal at around -45 degrees longitude over time. This change is present even if we only look at counts from the hemisphere away from Mars, excluding a Mars related source.

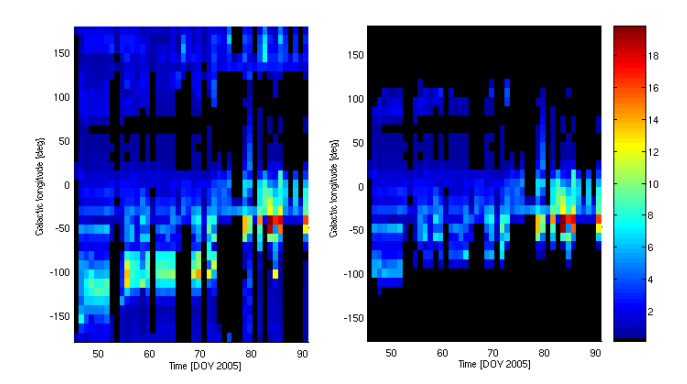


Fig. 10. Time evolution of the signal in the Galactic plane during 2005. Identical format as in Fig. 9 but for the Galactic plane, and with Galactic longitude and latitude. To the right, all observations in the hemisphere of directions centered at Mars were removed.

5. Discussion

The NPI has observed ENA and UV fluxes in the shadow of Mars in 2004 and 2005. The position of most of the strongest emissions in the NPI sky maps correspond fairly well to UV sources, but there is at least one signal that shifts position between the years, indicating that there are ENAs in this signal and that the ENAs seem not to be related to the Mars-solar wind interaction (they are well away from the Mars direction). In addition, there are ENAs seen in the eclipse that emanates from the Mars-solar wind interaction judging from the direction they come from (near Mars' limb).

There does not seem to be any obvious correlation between the NPI observations and the neutral streams discussed by Collier et al¹⁰., since those fluxes have incoming directions of 260-290 degrees ecliptic longitude, and we have not identified any possible neutral atom fluxes from these directions in the NPI data. However, all previous observations of interplanetary ENAs are indirect (except the ISN observations⁹). Thus, it is difficult to rule out that there is a connection between the NPI observations and previous observations.

12

The next step in this investigation is to identify features that change over time and examine the response of individual sectors to these signals, and how they vary over time. Also, one should investigate if any such signal can be identified in MEX NPD or IMAGE LENA data (this would confirm that a signal is interplanetary since IMAGE is in Earth orbit), detectors that are not UV sensitive. Since these detectors also have velocity resolution, we could get more information on the ENA populations seen. A future comparison with measurements by the ASPERA-4 NPI sensor onboard ESA's Venus Express mission could also confirm or rule out a possible interplanetary ENA signal. Venus Express is scheduled to arrive at the planet in April 2006.

6. Acknowledgment

We thank Teemu Mäkinen at the Finnish Meteorological Institute (FMI), and the SWAN team, for providing UV all-sky data.

Appendix A. NPI Angular and Energy Response

Here we present the NPI angular response, as used in the smoothing of the UV skymap in Figure 7. The angular response was measured during on-ground calibrations with an MCP bias voltage of -2500 V and is shown in Table 3.

We also show the NPI energy response from calibrations in Figure 11. Given an inter-sector normalized count rate, v_i , as defined in Table 2, we can estimate the incoming flux of neutrals as $f \approx v_i/(\epsilon G)$ [cm⁻²sr⁻¹s⁻¹], where the geometrical factor¹⁴ $G \approx 2.7 \cdot 10^{-3}$ [cm² sr], and ϵ is the energy dependent efficiency from Figure 11, e.g., for 1 keV neutrals we have $\epsilon \approx 4 \cdot 10^{-4}$, so a count rate of one per second would correspond to a flux of $2 \cdot 10^5$ [cm⁻²sr⁻¹s⁻¹].

References

- S. Barabash, R. Lundin, H. Andersson, J. Gimholt, M. Holmström, O. Norberg, M. Yamauchi, K. Asamura, A.J. Coates, D.R. Linder, et al., in A. Wilson, Ed., *Mars Express: The scientific payload*, ESA Special Publication, SP-1240, 121–139 (2004).
- 2. S. Barabash, R. Lundin, T. Zarnowiecki and S. Grzedzielski, Adv. Space Res., 16, 81–86 (1995).
- S. Barabash, O. Norberg, R. Lundin, S. Olsen, K. Lundin, P. C:Son Brandt, E.C. Roelof, C.J. Chase, B.H. Mauk, H. Koskinen et al., Measurement Techniques in Space Plasmas, Eds. Robert F. Pfaff et al., AGU, 257– (1998).

The NPI response azimuth-elevation, 31×14 , matrix for one sector. The unit is arbitrary, and normalized to a entry by that number. We define the boresight direction at the maximum element, (17,8). The step in azimuth and elevation is one degree, so element (i,j) at row i, column j, gives the response in azimuth i-17 degrees, and elevation j-8 degrees maximum value of 1. The sum of all entries is 82.0539, so to get a smoothing mask with a unit sum we should divide each 0.0150.0160.0380.030 0.0150.0150.046 0.0230.053 $0.023 \\ 0.007$ 0.008 0.008 0.000 0.016 0.018 0.000 0.0220.038 0.0390.031 0.0470.0250.0340.034 0.008 0.071 0.0160.0160.030 0.0380.030 0.0380.0620.0540.0390.070 0.0550.0550.0570.0230.0140.0590.0490.0090.0550.023 0.0470.0220.017 0.071 0.0170.1000.0990.0850.1070.0830.1090.0790.061 0.1020.0940.0950.0620.0810.030 0.0470.0820.0860.040 0.0500.0300.0320.0090.0080.0390.091 0.0340.0250.0080.203 0.2300.2990.2560.1950.2480.2270.2260.2370.2660.2750.2140.1860.1640.2270.2770.117 0.1290.0920.1040.0680.081 0.3190.4220.2850.3690.3720.5680.5030.5400.2340.312 0.1890.177 0.2370.2270.383 0.3650.3670.373 0.4230.4090.307 0.3350.2080.2260.2810.4750.6080.5470.6560.6170.2330.5160.5960.6630.8250.4430.5950.094 0.2220.5340.6410.4570.4940.701 0.621 0.3910.1620.4280.6280.6460.5630.6560.5830.5940.8260.8690.9651.000 0.8960.6120.8190.6250.5540.710 0.5250.5200.6880.6010.6010.420 0.2950.6680.5620.5020.5190.683 0.5520.717 0.8050.808 0.8750.6100.4540.3680.5370.4820.6250.4820.6810.571 0.821 0.418 0.4760.4900.306 0.4890.4170.5920.3530.4090.3200.3590.3560.2120.0840.084 0.2910.304 0.3810.434 0.4610.3650.2940.3880.2080.2160.1890.220 0.2320.2680.2430.2220.3150.2170.1590.0690.220 0.1370.270 0.1840.1830.2150.1920.2020.1960.0970.0840.1190.098 0.086 0.0380.1170.0890.0680.0620.0820.0450.0920.0830.0390.094 0.1270.082 0.0570.052 0.0450.0230.061 0.0540.077 0.1510.067relative the boresight direction. 0.047 0.0460.0150.0230.0230.0150.030 0.038 0.047 0.0390.047 0.073 0.0530.047 0.0520.047 0.0160.0360.015 0.030 0.031 0.0570.041 0.0370.026 0.031 0.032 0.030 0.0150.039 0.022 0.0220.0230.0150.015 0.0150.0150.047 0.029 0.008 0.008 0.008 0.008 0.008 0.007 0.0230.015 0.031 0.0240.037 0.0240.037 0.0270.031 0.031 Table 3. 0.0150.0150.0150.015 0.038 0.0220.023 0.015 0.0150.0150.007 0.0220.0150.0290.0160.007 0.030 0.031 0.000 0.0240.023 0.0240.000 0.008

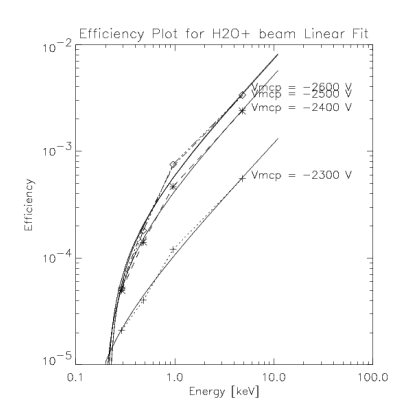


Fig. 11. The NPI efficiency to $\rm H_2O^+$ ions as a function of energy from on-ground calibrations. The different curves are for different MCP bias voltages. The in flight MCP bias voltage for the time period discussed here was -2400 V.

- H. Gunell, K. Brinkfeldt, M. Holmström, P. Brandt, S. Barabash, E. Kallio, A. Ekenbäck, Y. Futaana, R. Lundin, H. Andersson, et al., submitted to *Icarus* (2005).
- K. Brinkfeldt, H. Gunell, P.C. Brandt, S. Barabash, R.A. Frahm, J.D. Winningham, E. Kallio, M. Holmström, Y. Futaana, A. Ekenbäck, et al., submitted to *Icarus* (2005).
- E. Kallio, S. Barabash, K. Brinkfeldt, H. Gunell, M. Holmström, Y. Futaana,
 W. Schmidt, T. Säles, H. Koskinen, P. Riihelä, et al., submitted to *Icarus* (2005).
- 7. M. Holmström, S. Barabash and E. Kallio, J. Geophys. Res., 107, 10 (2002).
- 8. S. Barabash, M. Holmström, A. Lukyanov and E. Kallio, *J. Geophys. Res.*, 107, 10 (2002).
- 9. M. Witte, M. Banaszkiewicz, H. Rosenbauer, and D. McMullin, *Adv. Space Res.*, **34**, 61–65 (2004).
- M.R. Collier, T.E. Moore, D. Simpson, A. Roberts, A. Szabo, S. Fuselier, P. Wurz, M.A. Lee, and B.T. Tsurutani, Adv. Space Res., 34, 1, 166–171 (2004).
- 11. C.H. Acton, Planet. Space Sci., 44, 1, 65-70 (1996).
- T.E. Moore, D.J. Chornay, M.R. Collier, F.A. Herrero, J. Johnson, M.A. Johnson, J.W. Keller, J.F. Laudadio, J.F. Lobell, K.W. Ogilvie, et al., Space Sci. Rev., 91, 155-195 (2000).
- J.L. Bertaux, E. Kyrola, E. Quemerais, R. Pellinen, R. Lallement, W. Schmidt, M. Berthe, E. Dimarellis, J.P. Goutail, C. Taulemesse, et al., Sol. Phys., 162, 403–439 (1995).
- 14. K. Brinkfeldt, Instrumentation for energetic neutral atom measurements at Mars, Venus, and the Earth, Doctoral Thesis, Umeå University, Sweden (2005).